

# Epitaxial stabilization of pulsed laser deposited $\text{Sr}_{n+1}\text{Ir}_n\text{O}_{3n+1}$ thin films: entangled effect of growth dynamics and strain

Araceli Gutiérrez-Llorente,<sup>1,\*</sup> Lucía Iglesias,<sup>2</sup> Benito Rodríguez-González,<sup>3</sup> and Francisco Rivadulla<sup>2</sup>

<sup>1</sup>Universidad Rey Juan Carlos, Escuela Superior de Ciencias Experimentales y Tecnología, Madrid 28933, Spain

<sup>2</sup>Centro Singular de Investigación en Química Biolóxica e Materiais Moleculares (CiQUS),

Departamento de Química-Física, Universidade de Santiago de Compostela. 17582 Santiago de Compostela (Spain)

<sup>3</sup>Departamento de Química Física, Universidad de Vigo, 36310 Vigo, Spain

The subtle balance of electronic correlations, crystal field splitting and spin-orbit coupling in layered  $\text{Ir}^{4+}$  oxides can give rise to novel electronic and magnetic phases. Experimental progress in this field relies on the synthesis of epitaxial films of these oxides. However, the growth of layered iridates with excellent structural quality is a great experimental challenge. Here we selectively grow high quality single-phase films of  $\text{Sr}_2\text{IrO}_4$ ,  $\text{Sr}_3\text{Ir}_2\text{O}_7$ , and  $\text{SrIrO}_3$  on various substrates from a single  $\text{Sr}_3\text{Ir}_2\text{O}_7$  target by tuning background oxygen pressure and epitaxial strain. We demonstrate a complex interplay between growth dynamics and strain during thin film deposition. Such interplay leads to the stabilization of different phases in films grown on different substrates under identical growth conditions, which cannot be explained by a simple kinetic model. We further investigate the thermoelectric properties of the three phases and propose that weak localization is responsible for the low temperature activated resistivity observed in  $\text{SrIrO}_3$  under compressive strain.

## I. INTRODUCTION

Transition-metal oxides with partially filled  $d$ -electron states exhibit exceptionally rich electronic and magnetic phase diagrams.<sup>1–3</sup> Strong Coulomb interactions in narrow  $3d$ -bands can lead to Mott insulators ground states. Moving down into  $5d$  transition metal ions, the spatial extent of the orbitals increases, resulting in a stronger  $5d$ - $\text{O}:2p$  overlap. This widens the electronic bands, thus reducing electronic correlations, whereas the contribution of the crystal-field energy,  $\Delta$ , increases. Moreover, the higher atomic number results in a significant contribution of the spin-orbit coupling (SOC) energy. As a result,  $5d$ -Iridium ( $\text{Ir}^{4+}$ ) oxides constitute a family of materials in which SOC,  $\Delta$ , and electronic correlations present a comparable magnitude. Within this context, it has been proposed that SOC splits the threefold degenerate  $t_{2g}$  band in  $\text{Sr}_2\text{IrO}_4$  into a lower  $J_{\text{eff}}=3/2$  band, and a half-filled  $J_{\text{eff}}=1/2$  band. Coulomb interactions or additional structural distortions introduce further splitting in that narrow  $J_{\text{eff}}=1/2$  band, opening up a charge gap, which can be manipulated by epitaxial strain.<sup>4–13</sup>

The Ruddlesden-Popper (RP) series of strontium iridates,  $\text{Sr}_{n+1}\text{Ir}_n\text{O}_{3n+1}$ , features a localized-to-itinerant crossover from that insulating ground state of  $\text{Sr}_2\text{IrO}_4$  (with a two dimensional  $\text{IrO}_6$  corner-sharing octahedral network characteristic of  $n = 1$ ) to a correlated metallic state in the three dimensional perovskite  $\text{SrIrO}_3$  ( $n = \infty$ ).<sup>14</sup> This suggests the possibility of fine-tuning the charge gap across  $\text{Sr}_{n+1}\text{Ir}_n\text{O}_{3n+1}$  by growing high quality epitaxially strained thin films. Theoretically, tensile strain brings about an increase of the Ir-O-Ir bond angle that could favour larger bandwidths and conductivity, at least for  $n = 1$ .<sup>11</sup> In such case, Serrao et al.<sup>12</sup> proposed that the charge gap in  $\text{Sr}_2\text{IrO}_4$  depends on the ratio  $c/a$  of lattice parameters. But, as  $n$  increases the hopping along the  $c$ -axis becomes more relevant, and thus

such a simple analysis might be no longer adequate for other members of the RP series.

High-quality films are required to elucidate these compelling questions, making indispensable a precise control of the growth process. But, as the unit cell of each member of the RP series is a superlattice that consists of ordered sequences of perovskite layers ( $\text{SrIrO}_3$ ) sandwiched between two rock salt layers ( $\text{SrO}$ ) along the  $c$  crystallographic axis, intergrowth of different members is frequently found.<sup>15,16</sup> This renders the growth of such artificial layered phases a great experimental challenge, and their growth mechanisms, intriguing.<sup>17,18</sup>

Here we report the selective growth of high quality single-phase films of  $\text{Sr}_2\text{IrO}_4$ ,  $\text{Sr}_3\text{Ir}_2\text{O}_7$ , and  $\text{SrIrO}_3$  by pulsed laser deposition (PLD) from a single polycrystalline  $\text{Sr}_3\text{Ir}_2\text{O}_7$  target on substrates that impose different sign and degree of strain. The growth of RP phases on  $\text{SrTiO}_3$  substrates from a  $\text{SrIrO}_3$  or  $\text{Sr}_2\text{IrO}_4$  target has been reported by Nishio *et al.*<sup>20</sup> and by Liu *et al.*<sup>21</sup>, respectively. In this work, unlike these previous studies, we explore the impact of the strain imposed by the substrate on the growth of different phases. We demonstrate a complex interplay between strain and oxygen pressure during growth that can lead to the stabilization of different RP phases in films grown on different substrates under identical deposition conditions of laser fluence, substrate temperature, and background oxygen pressure. We also discuss the effect of strain, oxygen pressure, and dimensionality on the temperature dependence of thermoelectric power, electrical resistivity, and magnetization of these materials.

## II. RESULTS AND DISCUSSION

We grew 20 nm thick films of  $\text{Sr}_{n+1}\text{Ir}_n\text{O}_{3n+1}$  with  $n=1, 2$  and  $\infty$  on (001) $\text{SrTiO}_3$  (STO), (001)( $\text{LaAlO}_3$ )<sub>0.3</sub>( $\text{Sr}_2\text{AlTaO}_6$ )<sub>0.7</sub> (LSAT), and

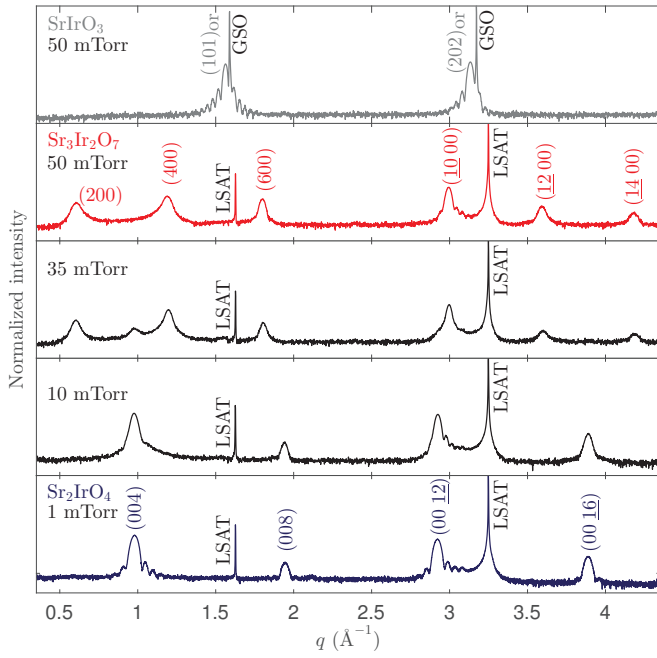


FIG. 1. Epitaxial thin films of  $n = 1, 2, \infty$  phases of  $\text{Sr}_{n+1}\text{Ir}_n\text{O}_{3n+1}$  series grown from a single  $\text{Sr}_3\text{Ir}_2\text{O}_7$  target. (a) Indexed XRD  $\theta$ - $2\theta$  scans of films grown on LSAT over an oxygen pressure range of 1 mTorr to 50 mTorr (from bottom to top), and on GSO at 50 mTorr (upper panel). Substrate temperature was 800 °C. As a rule, increasing the oxygen pressure promotes the stability of phases with larger  $n$ . The film grown at 35 mTorr on LSAT shows features that can be attributed to both  $n=1$  and  $n=2$  RP phases, suggesting a gradual transformation between the two phases. Noteworthy,  $\text{Sr}_3\text{Ir}_2\text{O}_7/\text{LSAT}$  and  $\text{SrIrO}_3/\text{GSO}$  are both grown on different substrates side by side in the PLD chamber. (see Fig. S1<sup>19</sup> for structural characterization of  $\text{Sr}_2\text{IrO}_4$  and  $\text{Sr}_3\text{Ir}_2\text{O}_7$  phases on STO substrates; Fig. S2<sup>19</sup> for  $\theta$ - $2\theta$  scans of  $\text{SrIrO}_3/\text{GSO}$  films grown at oxygen pressure in the range 35 mTorr to 100 mTorr; and, Fig. S3<sup>19</sup> and Fig. S4<sup>19</sup> that provide evidence of the influence of substrate on the stabilization of RP phases in films grown under identical deposition conditions).

(110)GdScO<sub>3</sub> (GSO) substrates by PLD from a single polycrystalline target of  $\text{Sr}_3\text{Ir}_2\text{O}_7$ . The laser fluence was optimized at  $\approx 1 \text{ J/cm}^2$ , and kept constant throughout the work. (See supplementary material for a detailed experimental description<sup>19</sup>).

Off-stoichiometric transfer of material from a multi-component oxide target to the substrate in pulsed PLD is an undeniable fact.<sup>16,26,27</sup> It is widely accepted that the angular distribution of the species attaining the substrate is modified as a result of the atomic collisions between the atoms of the plume and the molecules of the gas,<sup>28,29</sup> and changes in the oxygen background pressure can lead to a changeover in the growth mode.<sup>30,31</sup> Furthermore, epitaxial strain has a major impact on growth dynamics as it modifies surface diffusion and mobility of adatoms, although the character of that shift is strongly material dependent, and has been little explored in oxides.<sup>31-35</sup>

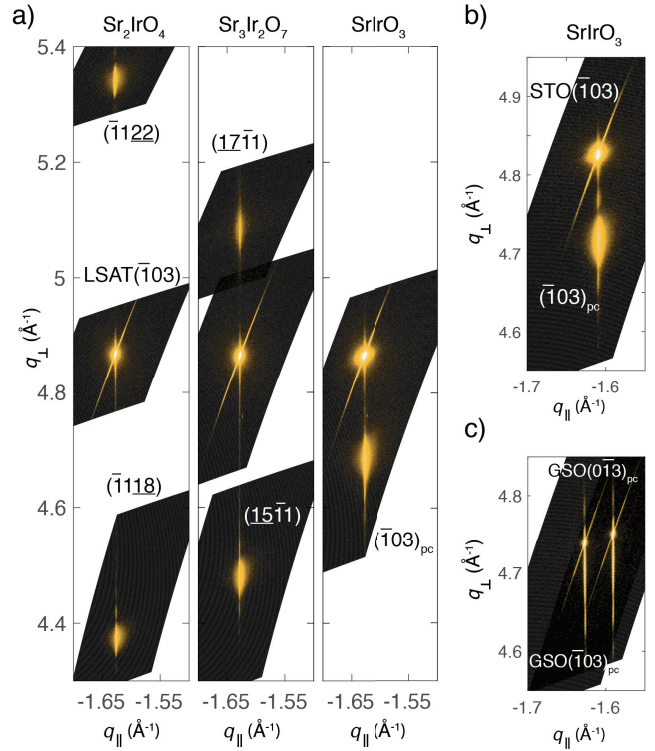


FIG. 2. a) High-resolution RSMs of  $\text{Sr}_2\text{IrO}_4$ ,  $\text{Sr}_3\text{Ir}_2\text{O}_7$ , and  $\text{SrIrO}_3$  on LSAT. The  $(\bar{1}03)$  reflection from the LSAT substrate is also shown in each map. b, c) RSMs around the  $(\bar{1}03)$  substrate reflection for films grown on STO(001) and GSO(110)<sub>OR</sub>, respectively. The pseudocubic reflections  $(\bar{1}03)_{pc}$  and  $(0\bar{1}3)_{pc}$  in  $\text{SrIrO}_3/\text{GSO}$  are observed at different  $(q_{\parallel}, q_{\perp})$  (c). This is consistent with the deviation of  $\beta$  from 90° that takes account of the orthorhombic distortion in the perovskite.

Fig. 1 shows x-ray diffraction (XRD)  $\theta$ - $2\theta$  scans of films grown on LSAT at an oxygen pressure of 1 mTorr, 10 mTorr, 35 mTorr and 50 mTorr, and on GSO at 50 mTorr, at a substrate temperature of 800 °C. The patterns of films grown at 1 mTorr and 50 mTorr on LSAT, and at 50 mTorr on GSO show all the peaks of  $\text{Sr}_2\text{IrO}_4$ ,  $\text{Sr}_3\text{Ir}_2\text{O}_7$ , and  $\text{SrIrO}_3$ , respectively, oriented with the long axis along the substrate normal. There is no hint of impurity phases in these patterns which suggests that the sequence of perovskite and rocksalt layers are correctly ordered in the periodic structures along the out-of-plane direction (see discussion of Transmission Electron Microscopy data below). Strong Laue thickness fringes surrounding the main Bragg peak give evidence of an excellent structural quality of these films. Rocking curve measurements for the  $(00\bar{1}2)\text{Sr}_2\text{IrO}_4$  peak show a FWHM of  $0.02^\circ \pm 0.003^\circ$  and  $0.06^\circ \pm 0.005^\circ$  for the films grown on LSAT substrates under 1 mTorr and 10 mTorr, respectively. The FWHM of the  $(002)_{OR}\text{SrIrO}_3$  peak of the film grown on GSO under 50 mTorr is  $0.05^\circ \pm 0.003^\circ$ . The diffraction peaks of  $\text{Sr}_2\text{IrO}_4$  can be indexed to the tetragonal unit cell:  $a = 5.499 \text{ \AA}$  and  $c = 25.784 \text{ \AA}$ , space

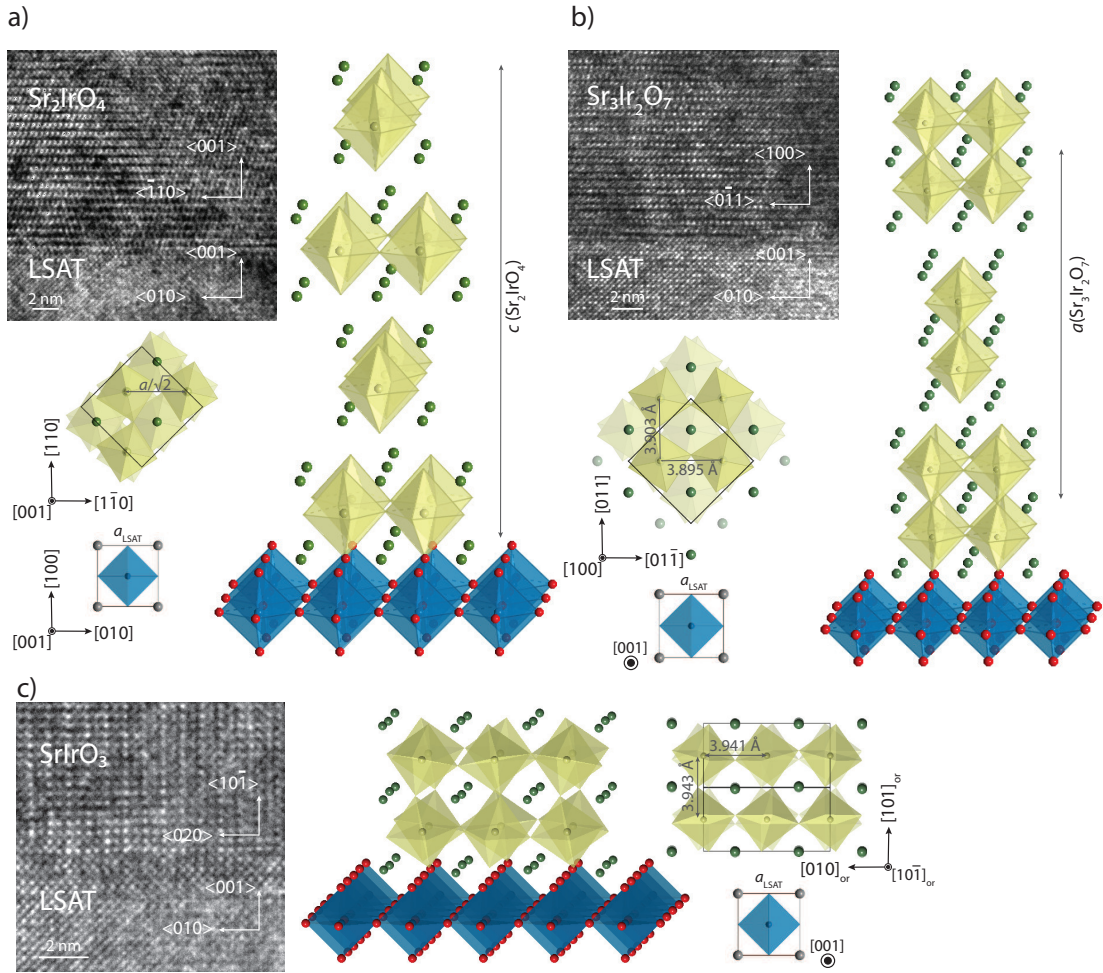


FIG. 3. High Resolution Transmission Electron Microscopy (HRTEM) images and structural model of the films on LSAT. Each panel shows the HRTEM image of the interface film/substrate, the 3D structural model, and the in-plane view. The deduced epitaxial alignments are outlined on each image. a) Tetragonal<sup>22</sup>  $\text{Sr}_2\text{IrO}_4(001)\|\text{LSAT}(001)$ , where the unit cell of  $\text{Sr}_2\text{IrO}_4$  grows  $45^\circ$  rotated relative to the LSAT unit cell:  $[110]\text{Sr}_2\text{IrO}_4\|[100]\text{LSAT}$ . This enables lattice matching of  $a(\text{Sr}_2\text{IrO}_4)/\sqrt{2} = 3.888 \text{ \AA}$  with  $a(\text{LSAT})=3.868 \text{ \AA}$ . b)  $\text{Sr}_3\text{Ir}_2\text{O}_7(100)\|\text{LSAT}(001)$ , where  $\text{Sr}_3\text{Ir}_2\text{O}_7$  is depicted as a distorted perovskite (long axis along  $a$ <sup>23</sup>). This refined structure gives rise to an in-plane pseudocubic lattice of roughly  $3.90 \text{ \AA}$ . The unit cell of  $\text{Sr}_3\text{Ir}_2\text{O}_7$  phase also grows  $45^\circ$  rotated relative to the LSAT substrate:  $[011]\text{Sr}_3\text{Ir}_2\text{O}_7\|[100]\text{LSAT}$ . c) Orthorhombic  $\text{SrIrO}_3$  ( $b$  as long axis<sup>24,25</sup>) shows an epitaxial relationship of  $(10\bar{1})_{\text{or}}\|[101]_{\text{or}}\text{SrIrO}_3\|(001)[100]\text{LSAT}$ . The tetrahedral rotation patterns expected for each space group in bulk are depicted. See Supplementary Information for electron diffraction patterns (Fig. S5<sup>19</sup>).

group  $I4_1/acd$ .<sup>22</sup> The peaks observed in  $\text{Sr}_3\text{Ir}_2\text{O}_7$  are compatible with a subtly distorted perovskite described by a monoclinic space group ( $C2/c$ )<sup>23</sup> with parameters  $20.935 \text{ \AA}$ ,  $5.5185 \text{ \AA}$ , and  $5.5099 \text{ \AA}$ , where the long cell axis ( $a$  in the standard setting of space group  $C2/c$ ) is parallel to the surface normal. In this structure, a single oblique angle  $\beta=90.045^\circ$  produces a minute deviation from a quadratic lattice<sup>23</sup>, which is below our X-ray experimental resolution.  $\text{SrIrO}_3$  has been indexed to an orthorhombic perovskite cell with  $Pnma$  symmetry and lattice parameters  $a = 5.5909 \text{ \AA}$ ,  $b = 7.8821 \text{ \AA}$ , and  $c = 5.5617 \text{ \AA}$ <sup>24,25</sup> (pseudo-cubic unit cell of roughly  $3.94 \text{ \AA}$ ).

X-ray reciprocal space maps (RSMs) of the three phases on different substrates in Fig. 2 show that the

films are fully strained to the in-plane lattice parameter of the substrate. As expected, the out-of-plane lattice parameter of  $\text{Sr}_2\text{IrO}_4$  expands (shrinks) relative to that of bulk under in-plane compressive (tensile) strain induced by LSAT (STO) substrate. It decreases from  $25.86\pm 0.05 \text{ \AA}$  on LSAT to  $25.72\pm 0.03 \text{ \AA}$  on STO (tensile strain of  $\approx +0.64\%$ ). Likewise, in-plane tensile (compressive) strain also results in a contraction (expansion) along the out-of-plane direction in  $\text{Sr}_3\text{Ir}_2\text{O}_7$ . It shrinks along the  $c$ -axis from  $21.03\pm 0.03 \text{ \AA}$  under compressive strain on LSAT to  $20.81\pm 0.04 \text{ \AA}$  under tensile strain on STO. These values are in good agreement with values for the bulk of  $n=1$  and  $n=2$  RP phases.<sup>22,36</sup>

Further insight into the microstructure and composition of the films is provided by Transmission Electron

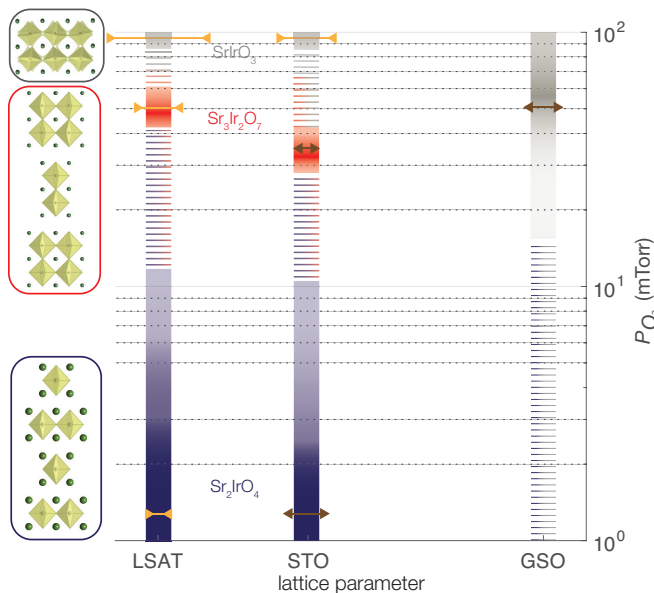


FIG. 4. Combined effect of epitaxial strain and background oxygen pressure from a single  $\text{Sr}_3\text{Ir}_2\text{O}_7$  target at a substrate temperature of  $800^\circ\text{C}$ . Vertical bars show the experimental oxygen pressure window for the stabilization of  $\text{Sr}_2\text{IrO}_4$  (blue),  $\text{Sr}_3\text{Ir}_2\text{O}_7$  (red) and  $\text{SrIrO}_3$  (grey) phases on LSAT, STO and GSO substrates. Films grown over the oxygen pressure range denoted by discontinuous stripes exhibit features of two phases. We were not able to grow the  $\text{Sr}_2\text{IrO}_4$  phase at low oxygen pressure on GSO substrates (see Supplementary Information, Fig. S6<sup>19</sup>). The pictures on the left illustrate the crystal structures of the three phases. Compressive (tensile) strain induced by the substrate on each structure is depicted by yellow (brown) arrows whose lengths are proportional to the magnitude of strain.

Microscopy (TEM) on cross-section lamellas (Fig. 3). In agreement with the RSM results, we find that the films are fully strained to the substrate. The analysis of the electron diffraction patterns (Fig. S5<sup>19</sup>) reveals in-plane orientation relationships for  $\text{Sr}_2\text{IrO}_4$  and  $\text{Sr}_3\text{Ir}_2\text{O}_7$  films where the unit cell of the iridate grows  $45^\circ$  rotated relative to the LSAT unit cell (Fig. 3(a, b)). Orthorhombic  $\text{SrIrO}_3$  ( $b$  as long axis) shows an epitaxial relationship of  $(10\bar{1})_{\text{or}}[101]_{\text{or}}\text{SrIrO}_3\parallel(001)[100]_{\text{LSAT}}$  (Fig. 3(c)). Semiquantitative Energy Dispersive Spectroscopy (EDS) analyses of the films confirmed a close to stoichiometric Sr/Ir ratio of 1.91, 1.74, and 1.12 for films grown under oxygen pressure of 1 mTorr, 50 mTorr and 100 mTorr, respectively.

Fig. 4 summarizes the entanglement of epitaxial strain and background oxygen pressure in the stabilization of  $\text{Sr}_{n+1}\text{Ir}_n\text{O}_{3n+1}$  phases. For example,  $\text{Sr}_2\text{IrO}_4$  grows with excellent structural quality on LSAT (small lattice mismatch  $\approx -0.26\%$ ) at oxygen pressure about 1 mTorr, as we have stated above. However, this phase does not stabilize under a strain of  $\approx +2\%$  (GSO substrate) over the range of oxygen pressures studied in this work (see Fig. S6<sup>19</sup>). Furthermore, we obtain single-phase

$\text{Sr}_3\text{Ir}_2\text{O}_7$  films at 50 mTorr on LSAT (lattice mismatch of  $\approx -0.75\%$ ); and, at 35 mTorr on STO (lattice mismatch  $\approx +0.15\%$ , Fig. S1<sup>19</sup>). Moreover,  $\text{SrIrO}_3$  grows with high structural quality tensile-strained ( $\approx +0.51\%$ ) on GSO already above  $\approx 40$  mTorr (see also Supplementary Information, Fig. S2<sup>19</sup>).

A picture emerges from these results: epitaxial stress plays a fundamental role in the stabilization of RP phases; and, low (high) oxygen partial pressure favours the formation of phases with high (low) Sr/Ir ratio. PLD plume dynamics can be invoked to give a first interpretation of these results. In a simple kinetic model, the plume species are expected to diffuse while interacting with the background gas until reaching the substrate. Given the large difference in size and mass between Ir and Sr, it is expected that background oxygen pressure will significantly affect propagation velocity and angular distribution of Ir and Sr species which, in turn, will impact on the Sr/Ir cation ratio of the films.

At the working laser fluence of  $\approx 1\text{ J/cm}^2$ , we observe that Sr is preferentially ablated from the target, as proved by EDS analysis carried out on the target. The original stoichiometric Sr/Ir ratio is recovered after careful polishing of the surface of the target. We grew the films after a long preablation of the target surface to ensure that a steady state had been reached. Such a preferential ablation of Sr has previously been reported for a  $\text{SrIrO}_3$  target at laser fluences varying from 0.4 to  $2.0\text{ J/cm}^2$ .<sup>37</sup>

At low background oxygen pressure, it is predicted that lighter Sr species outnumber heavier Ir species at the plume front.<sup>29</sup> This effect helps overcoming the Ir enrichment of the target surface owing to Sr preferential ablation. In fact, results of complementary growths hint that preferential ablation of Sr is not a key condition for the stabilization of the  $\text{Sr}_2\text{IrO}_4$  phase at low oxygen pressure (see Fig. S7<sup>19</sup>, and discussion in Supplementary Information). As a result, films with Sr/Ir ratio higher than that of the  $\text{Sr}_3\text{Ir}_2\text{O}_7$  polycrystalline target are grown at oxygen pressure around 1 mTorr on LSAT and STO substrates. As the oxygen pressure inside the chamber increases, the propagation behaviour of the species changes.<sup>30</sup> In this case, lighter and larger species, such as Sr, are preferentially scattered during their flight towards the substrate. Therefore, as the number of scattering events increases at high oxygen pressure, there is an enrichment in Ir along the direction normal to the substrate that leads to films with Sr/Ir ratio lower than that of the  $\text{Sr}_3\text{Ir}_2\text{O}_7$  target.

Fig. 5 shows the evolution of unit cell parameters of  $\text{SrIrO}_3$  as function of strain for samples synthesized under different temperatures and oxygen pressures. The values shown in Fig. 5 are in accordance with literature.<sup>13,37,38</sup> Under the optimized growth conditions, the tetragonal distortion,  $c/a$ , decreases with tensile strain, although at a lower rate than that expected assuming a Poisson's ratio of  $\nu = 0.3$ , a value common to other oxide-perovskites.<sup>39,40</sup> We find that the  $c/a$  ratio increases with increasing temperature (oxygen pressure) while keep-

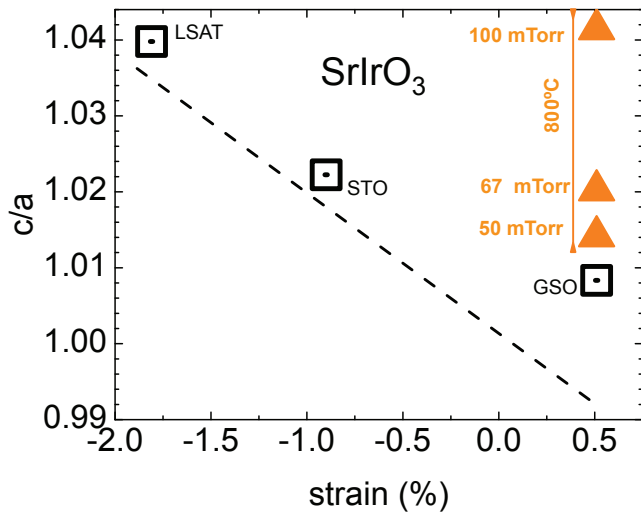


FIG. 5. Variation of the  $c/a$  ratio of pseudocubic lattice parameters with strain (open squares) and background oxygen pressure (solid triangles) of  $\text{SrIrO}_3$  films. The open squares correspond to samples synthesized at 67 mTorr and 700°C in the same batch. The triangles correspond to samples deposited on GSO at 800°C, under different oxygen pressures (this data are extracted from XRD  $\theta$ - $2\theta$  scans shown in Fig. S2 and Fig. S8<sup>19</sup>). The dotted line corresponds to  $c/a$  calculated for a Poisson's ratio of  $\nu=0.3$ .

ing the oxygen pressure (temperature) constant. For instance, the film grown at the highest pressure (100 mTorr) exhibits the highest  $c/a$  ratio. Thus, we exclude the presence of oxygen vacancies as the cause of the deformation of the unit cell of  $\text{SrIrO}_3$  depicted in Fig. 5.<sup>41,42</sup> Instead the behaviour of  $c/a$  has to be caused by an increase of cation vacancies with increasing temperature and/or oxygen pressure. The preferential scattering of Sr in the plume at high oxygen pressure predicted by the kinetic model described above would result in  $\text{SrIrO}_3$  films with an increased concentration of Sr vacancies, giving rise to the cell expansion observed in Fig. 5 for the films grown under tensile strain.

In addition, transport properties of epitaxially grown  $\text{SrIrO}_3$  films are significantly affected by non-stoichiometric Sr/Ir ratio. Indeed, the  $\text{SrIrO}_3$  film grown on GSO at 800°C and 100 mTorr of oxygen pressure exhibits semiconducting-like behaviour (Fig. S9<sup>19</sup>) which can be associated with the increase of Sr vacancies postulated above. A film of  $\text{SrIrO}_3$  grown from a target with higher Sr/Ir ratio under identical conditions of substrate temperature and oxygen pressure exhibits metallic behaviour (Fig. S10.<sup>19</sup>), supporting the picture of Anderson-like localization by vacancy scattering.

On the other hand, such a simple model of PLD plume dynamics overlooks the influence of epitaxial strain on diffusion of species at the substrate surface. Actually, we observe that epitaxial strain can promote the stabilization of different phases in films grown on different substrates under identical growth conditions of laser flu-

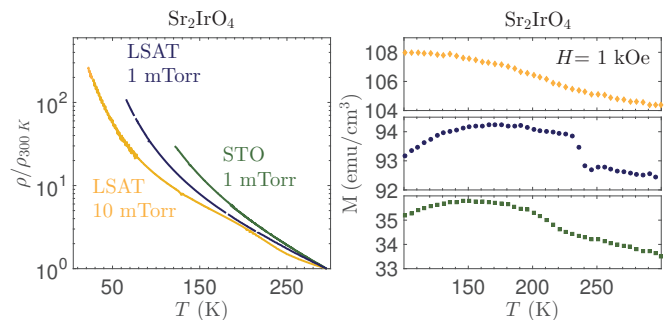


FIG. 6. Left panel: temperature dependence of electrical resistivity,  $\rho(T)$ , normalized to room temperature of  $\text{Sr}_2\text{IrO}_4$  films grown at 800°C on LSAT at 1 mTorr (blue), LSAT at 10 mTorr (yellow), and STO at 1 mTorr (green). Right panel: temperature dependence of magnetization,  $M(T)$ , at  $H=1$  kOe of the same films.

ence, substrate temperature, and oxygen pressure (Fig. 1 and Fig. S4<sup>19</sup>). For instance, it has been reported that tensile epitaxial strain brings about an energy barrier for adatom diffusion during the growth of complex oxides at low oxygen pressures by PLD.<sup>31</sup> We hypothesize this decrease of surface diffusion and mobility of adatoms hinders the growth of  $\text{Sr}_2\text{IrO}_4$  and  $\text{Sr}_3\text{Ir}_2\text{O}_7$  phases on GSO substrates. It is also worth bearing in mind that  $\text{SrIrO}_3$  has lower lattice mismatch with GSO,  $\approx +0.51\%$ , than  $\text{Sr}_2\text{IrO}_4$  ( $\approx +2\%$ ) or  $\text{Sr}_3\text{Ir}_2\text{O}_7$  ( $\approx +1.6\%$ ), providing the driving force for the stabilization of  $\text{SrIrO}_3$  if growth conditions of substrate temperature or oxygen pressure make it possible.

Therefore, both kinetic and thermodynamic aspects are relevant to explain the stabilization of the different phases reported in this work (see supplementary material<sup>19</sup> for a description of the impact of volatile  $\text{IrO}_2$ ). Additional experiments to probe the angular distribution of Sr and Ir species in the plume, and to further understand the role played by oxygen on the plume propagation dynamics and on the incorporation of volatile species into the film would be highly interesting.

Fig. 6 summarizes the effect of background oxygen pressure, and strain on magnetic and transport properties of  $\text{Sr}_2\text{IrO}_4$ . This phase remains semiconducting irrespective of oxygen pressure and strain, not showing any sensitivity to the magnetic transition, as expected.<sup>43,44</sup> In contrast, as the canting of Ir magnetic moments in  $\text{Sr}_2\text{IrO}_4$  follow the  $\text{IrO}_6$  octahedral rotations,<sup>45-47</sup> epitaxial strain is expected to have a strong influence on its magnetic properties. We observe a sharp magnetic transition around  $T \approx 240$  K (bulk value<sup>5</sup>) for the film grown compressively strained on LSAT at the lowest oxygen pressure, 1 mTorr. This transition is flattened in the film grown on LSAT at 10 mTorr, resulting from a decreased structural quality of the films grown at higher pressures. Indeed, rocking curves around the  $(00\bar{1}2)\text{Sr}_2\text{IrO}_4$  peak exhibit a FWHM of  $0.02^\circ \pm 0.003^\circ$  or  $0.06^\circ \pm 0.005^\circ$  for films grown under 1 mTorr or 10 mTorr, respectively, while no significant difference was found in the out-of-

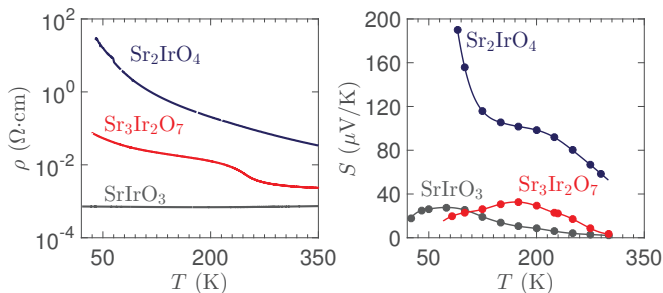


FIG. 7. Temperature dependence of the electrical resistivity,  $\rho(T)$ , and Seebeck coefficient,  $S(T)$ , of  $\text{Sr}_2\text{IrO}_4$ ,  $\text{Sr}_3\text{Ir}_2\text{O}_7$ , and  $\text{SrIrO}_3$  films grown on LSAT(001). The lines in the Seebeck figure are a guide to the eye.

plane lattice parameter between both films ( $25.86 \pm 0.05$  Å and  $25.85 \pm 0.06$  Å, respectively). We also find that the ferromagnetic component, which stems from the canted antiferromagnetic order, is lower in the film grown on STO (tensile strain) than in those grown on LSAT (compressive strain). This is in accordance with previous studies on 200 nm-thick  $\text{Sr}_2\text{IrO}_4$  films where higher tensile strain was reported to lead to lower octahedral rotation, resulting in a weaker ferromagnetic component.<sup>48</sup>

The temperature dependence of resistivity,  $\rho(T)$ , and Seebeck coefficient,  $S(T)$ , of  $\text{Sr}_2\text{IrO}_4$ ,  $\text{Sr}_3\text{Ir}_2\text{O}_7$ , and  $\text{SrIrO}_3$  on LSAT are shown in Fig. 7. Epitaxial compression on LSAT increases with increasing dimensionality of the material,  $n$ . Electrical transport of these phases is consistent with the widely accepted bandwidth-driven insulator-to-metal transition previously reported on the  $\text{Sr}_{n+1}\text{Ir}_n\text{O}_{3n+1}$  series as a result of increasing dimensionality,  $n$ :  $\text{Sr}_2\text{IrO}_4/\text{LSAT}(001)$  shows semiconducting behavior and high resistivity;  $\text{Sr}_3\text{Ir}_2\text{O}_7/\text{LSAT}(001)$  exhibits a semiconducting-like behavior over the whole range of temperature with a characteristic feature that reflects the antiferromagnetic transition expected at  $T = 285$  K in bulk;<sup>49</sup> and,  $\text{SrIrO}_3/\text{LSAT}(001)$  presents a very low resistivity and metallic behavior, with a slight upturn at low temperatures.

The Seebeck coefficient of the films on LSAT is positive in the whole range of temperatures measured, Fig. 7. The magnitude of  $S(T)$  in  $\text{Sr}_2\text{IrO}_4$  is in accordance with previous reports on polycrystalline<sup>15,50</sup> and single-crystal samples.<sup>43,44</sup> We observed a clear plateau below  $\approx 200$  K for the epitaxial films that could be linked to the canted antiferromagnetic structure reported in bulk,<sup>5,45</sup> although no anomaly of the Seebeck coefficient at the magnetic transition temperature has been observed in single crystals<sup>43,44</sup> or polycrystalline<sup>15,50</sup>  $\text{Sr}_2\text{IrO}_4$ . We are not aware of any other measurements of the thermoelectrical properties of epitaxial films of  $\text{Sr}_2\text{IrO}_4$  or  $\text{Sr}_3\text{Ir}_2\text{O}_7$ .

The effect of epitaxial strain on the thermoelectric properties of  $\text{SrIrO}_3$  is shown in Fig. 8. These films were prepared in the same batch. Thus, the dissimilarity in their electronic properties must stem from different

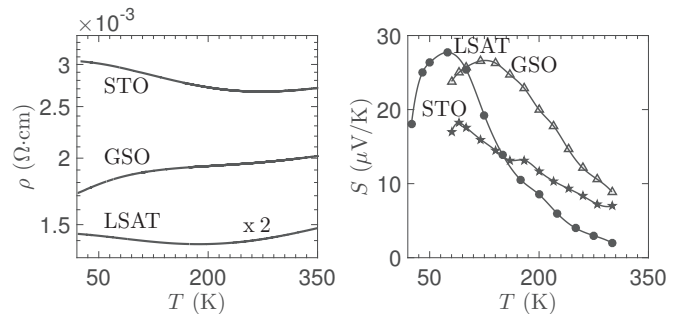


FIG. 8. Temperature dependence of the electrical resistivity,  $\rho(T)$ , and Seebeck coefficient,  $S(T)$ , of  $\text{SrIrO}_3$  films grown on GSO ( $\Delta$ ), STO ( $*$ ) and LSAT ( $\circ$ ). These films were grown in the same batch (67 mTorr,  $700^\circ\text{C}$ ). The resistivity of the film grown on LSAT has a scale factor of 2. The lines in the Seebeck figure are a guide to the eye. (See Fig. S8<sup>19</sup> for XRD measurements of the films).

substrate induced strain:  $-1.8\%$ ,  $-0.9\%$  and  $+0.5\%$  for LSAT, STO and GSO, respectively. Moreover, electrical transport measurements were carried out immediately after growth for three days in a row hence, degradation effects reported to occur in the  $\text{SrIrO}_3$  films<sup>37</sup> are expected to be negligible. The temperature dependence of  $\rho(T)$  shows metallic behavior at high temperature, with a crossover towards a thermally activated state defined by  $(d\rho(T)/dT) < 0$  at low temperature in the samples under compressive strain. The magnitude of the  $\rho(T)$  and the value of the crossover temperature do not follow any clear dependence with the  $c/a$  ratio. Therefore, they cannot be directly related to a change in bandwidth with strain.

This is in contrast to previous studies about the strain effect on electrical transport in  $\text{SrIrO}_3$  films.<sup>13,51</sup> These studies suggested a bandwidth controlled via strain model, according to which the Ir-O-Ir angle decreases (increases) by compressive (tensile) strain (while Ir-O length is not modified), thus shrinking (expanding) the bandwidth. Such scenario echoes the behavior observed in  $\text{Sr}_2\text{IrO}_4$ ,<sup>12</sup> but essential differences between  $\text{Sr}_2\text{IrO}_4$  and  $\text{SrIrO}_3$  have been pointed out. In particular,  $\text{SrIrO}_3$  exhibits out-of-plane octahedral rotations along the [110] pseudocubic direction, but no such [110] rotations are found experimentally in  $\text{Sr}_2\text{IrO}_4$ .<sup>38</sup> Furthermore, a reported narrower bandwidth in  $\text{SrIrO}_3$  than in  $\text{Sr}_2\text{IrO}_4$  casts doubt on the conventional picture of increased bandwidth with increasing dimensionality,  $n$ , in the RP series of iridates.<sup>38</sup> On the other hand, the Seebeck coefficients are very similar for all  $\text{SrIrO}_3$  films, with only a slight dependence on epitaxial strain, Fig. 8. As thermoelectric voltage is measured in open circuit conditions, no electrical current flows through the sample, and consequently  $S(T)$  is not as sensitive to grain boundaries and point-defect scattering as electrical resistivity. Indeed,  $S(T)$  rather depends on the intrinsic electronic structure of the conductor. Therefore, we suggest that localization induced by disorder is responsible for the tem-

perature dependence of the resistivity observed in these films. This is in agreement with previous observations of a persistent Drude-like peak in the optical conductivity of SrIrO<sub>3</sub> films under comparable strain.<sup>13</sup>

### III. CONCLUSIONS

Our results reveal an intricate coupling between epitaxial strain and oxygen pressure during pulsed laser deposition of Sr<sub>n+1</sub>Ir<sub>n</sub>O<sub>3n+1</sub> films. Such coupling suggests the possibility of growing artificial superlattices of iridates with tailored electronic and magnetic properties by varying the background pressure during deposition.<sup>52,53</sup> In addition, future works could address atomic-scale effects of strain on the surface diffusion of species during growth, and the influence of the oxidation state of the arriving species to promote the stabilization of RP phases with different cation stoichiometry.<sup>17,18,31,54</sup> This study would require *in-situ* characterization to monitor the film growth, and would provide fundamental insights into the growth process that may lead to the stabilization of new phases of layered materials. We have also shown that weak localization effects owing to accommodation

to compressive epitaxial strain dominate the conductivity of the metallic SrIrO<sub>3</sub> films, beyond the simple model of bandwidth controlled via strain.

### SUPPLEMENTARY MATERIAL

See supplementary material for a detailed experimental description, additional figures, and a comment on the impact of volatile IrO<sub>2</sub>.

### ACKNOWLEDGMENTS

This work has received financial support from Ministerio de Economía y Competitividad (Spain) under project No. MAT2016-80762-R, Xunta de Galicia (Centro singular de investigación de Galicia accreditation 2016-2019, ED431G/09) and the European Union (European Regional Development Fund-ERDF).

A.G.L. acknowledges financial support from Universidad de Santiago de Compostela. L.I. also acknowledges Mineco-Spain for support under a FPI grant.

\* araceli.gutierrez@urjc.es

<sup>1</sup> J. B. Goodenough, Magnetism and the Chemical Bond (John Wiley and Sons, New York, 1963).

<sup>2</sup> M. Imada, A. Fujimori, and Y. Tokura, Reviews of Modern Physics **70** (1998), 10.1103/RevModPhys.70.1039.

<sup>3</sup> Y. Tokura and N. Nagaosa, Science **288** (2000), 10.1126/science.288.5465.462.

<sup>4</sup> B. J. Kim, H. Jin, S. J. Moon, J. Y. Kim, B. G. Park, C. S. Leem, J. Yu, T. W. Noh, C. Kim, S. J. Oh, J. H. Park, V. Durairaj, G. Cao, and E. Rotenberg, Physical Review Letters **101** (2008), 10.1103/PhysRevLett.101.076402.

<sup>5</sup> B. J. Kim, H. Ohsumi, T. Komesu, S. Sakai, T. Morita, H. Takagi, and T. Arima, Science **323** (2009), 10.1126/science.1167106.

<sup>6</sup> J. L. Lado and V. Pardo, Physical Review B **92** (2015), 10.1103/PhysRevB.92.155151.

<sup>7</sup> Z. T. Liu, M. Y. Li, Q. F. Li, J. S. Liu, W. Li, H. F. Yang, Q. Yao, C. C. Fan, X. G. Wan, Z. Wang, and D. W. Shen, Scientific Reports (2016), 10.1038/srep30309.

<sup>8</sup> Y. Okada, D. Walkup, H. Lin, C. Dhital, T. R. Chang, S. Khadka, W. W. Zhou, H. T. Jeng, M. Paranjape, A. Bansil, Z. Q. Wang, S. D. Wilson, and V. Madhavan, Nature Materials **12** (2013), 10.1038/nmat3653.

<sup>9</sup> Q. Wang, Y. Cao, J. A. Waugh, S. R. Park, T. F. Qi, G. C. O. B. Korneta, and D. S. Dessau, Physical Review B **87** (2013), 10.1103/PhysRevB.87.245109.

<sup>10</sup> B. M. Wojek, M. H. Berntsen, S. Boseggia, A. T. Boothroyd, D. Prabhakaran, D. F. McMorrow, H. M. Rønnow, J. Chang, and O. Tjernberg, Journal of Physics: Condensed Matter **24** (2012), 10.1088/0953-8984/24/41/415602.

<sup>11</sup> J. Nichols, J. Terzic, E. G. Bittle, O. B. Korneta, L. E. D. Long, J. W. Brill, G. Cao, and S. S. A. Seo, Applied Physics Letters **102** (2013), 10.1063/1.4801877.

<sup>12</sup> C. Rayan Serrao, J. Liu, J. T. Heron, G. Singh-Bhalla, A. Yadav, S. J. Suresha, R. J. Paull, D. Yi, J.-H. Chu, M. Trassin, A. Vishwanath, E. Arenholz, C. Frontera, J. Železný, T. Jungwirth, X. Marti, and R. Ramesh, Physical Review B **87** (2013), 10.1103/PhysRevB.87.085121.

<sup>13</sup> J. H. Gruenewald, J. Nichols, J. Terzic, G. Cao, J. W. Brill, and S. S. A. Seo, Journal of Materials Research **29** (2014), 10.1557/jmr.2014.288.

<sup>14</sup> S. J. Moon, H. Jin, K. W. Kim, W. S. Choi, Y. S. Lee, J. Yu, G. Cao, A. Sumi, H. Fujimori, C. Bernhard, and T. W. Noh, Physical Review Letters **101** (2008), 10.1103/PhysRevLett.101.226402.

<sup>15</sup> I. Pallecchi, M. T. Buscaglia, V. Buscaglia, E. Gilioli, G. Lamura, F. Telesio, M. R. Cimberle, and D. Marre, Journal of Physics-Condensed Matter **28** (2016), 10.1088/0953-8984/28/11/115602.

<sup>16</sup> S. S. A. Seo, J. Nichols, J. Hwang, J. Terzic, J. H. Gruenewald, M. Souri, J. Thompson, J. G. Connell, and G. Cao, Applied Physics Letters **109** (2016), 10.1063/1.4967450.

<sup>17</sup> J. H. Lee, G. Luo, I. C. Tung, S. H. Chang, Z. Luo, M. Malshe, M. Gadre, A. Bhattacharya, S. M. Nakhmanson, J. A. Eastman, H. Hong, J. Jellinek, D. Morgan, D. D. Fong, and J. Freeland, Nature Materials **13** (2014), 10.1038/nmat4039.

<sup>18</sup> Y. F. Nie, Y. Zhu, C. H. Lee, L. F. Kourkoutis, J. A. Mundy, J. Junquera, P. Ghosez, D. J. Baek, S. Sung, X. X. Xi, K. M. Shen, D. A. Muller, and D. G. Schlom, Nature Communications **5** (2014), 10.1038/ncomms5530.

<sup>19</sup> See supplementary material for a detailed experimental description, additional figures, and a comment on the impact of volatile IrO<sub>2</sub>.

<sup>20</sup> K. Nishio, H. Y. Hwang, and Y. Hikita, APL Materials **4** (2016), 10.1063/1.4943519.

- <sup>21</sup> X. Liu, Y. Cao, B. Pal, S. Middey, M. Kareev, Y. Choi, P. Shafer, D. Haskel, E. Arenholz, and J. Chakhalian, *Physical Review Materials* **1** (2017), 10.1103/PhysRevMaterials.1.075004.
- <sup>22</sup> Q. Huang, J. L. Soubeyroux, O. Chmaissem, I. N. Sora, A. Santoro, R. J. Cava, J. J. Krajewski, and W. F. P. Jr, *Journal of Solid State Chemistry* **112** (1994), 10.1006/jssc.1994.134110.
- <sup>23</sup> T. Hogan, L. Bjaalie, L. Zhao, C. Belvin, X. Wang, C. G. V. de Walle, D. Hsieh, and S. D. Wilson, *Physical Review B* **93** (2016), 10.1103/PhysRevB.93.134110.
- <sup>24</sup> J. G. Zhao, L. X. Yang, Y. Yu, F. Y. Li, R. C. Yu, Z. Fang, L. C. Chen, and C. Q. Jin, *Journal of Applied Physics* **103** (2008), 10.1063/1.2908879.
- <sup>25</sup> D. Puggioni and J. M. Rondinelli, *Journal of Applied Physics* **119** (2016), 10.1063/1.4942651.
- <sup>26</sup> S. Wicklein, A. Sambri, S. Amoruso, X. Wang, R. Bruzzese, A. Koehl, and R. Dittmann, *Applied Physics Letters* **101** (2012), 10.1063/1.4754112.
- <sup>27</sup> H. Schraknepper, C. Baumer, F. Gunkel, R. Dittmann, and R. A. D. Souza, *APL Materials* **4** (2016), 10.1063/1.4972996.
- <sup>28</sup> D. M. Packwood, S. Shiraki, and T. Hitosugi, *Physical Review Letters* **111** (2013), 10.1103/PhysRevLett.111.036101.
- <sup>29</sup> A. Sambri, C. Aruta, E. D. Gennaro, X. Wang, U. S. di Uccio, F. M. Granozio, and S. Amoruso, *Journal of Applied Physics* **119** (2016), 10.1063/1.4943589.
- <sup>30</sup> R. Groenen, J. Smit, K. Orsel, A. Vailionis, B. Bastiaens, M. Huijben, K. Boller, G. Rijnders, and G. Koster, *APL Materials* **3** (2015), 10.1063/1.4926933.
- <sup>31</sup> A. Tselev, R. K. Vasudevan, A. G. Gianfrancesco, L. Qiao, T. L. Meyer, H. N. Lee, M. D. Biegalski, A. P. Baddorf, and S. V. Kalinin, *Crystal Growth and Design* **16** (2016), 10.1021/acs.cgd.5b01826.
- <sup>32</sup> H. Brune, K. Bromann, H. Rder, K. Kern, J. Jacobsen, P. Stoltze, K. Jacobsen, and J. Norskov, *Physical Review B* **52** (1995), 10.1103/PhysRevB.52.R14380.
- <sup>33</sup> M. Schroeder and D. E. Wolf, *Surface Science* **375** (1997), 10.1016/S0039-6028(96)01250-2.
- <sup>34</sup> C. Xu, S. Wicklein, A. Sambri, S. Amoruso, M. Moors, and R. Dittmann, *J. Phys. D: Appl. Phys.* **47** (2014), 10.1088/0022-3727/47/3/034009.
- <sup>35</sup> S. Pandya, A. R. Damodaran, R. Xu, S. L. Hsu, J. C. Agar, and L. W. Martin, *Scientific Reports* **26075** (2016), 10.1038/srep26075.
- <sup>36</sup> M. A. Subramanian, M. K. Crawford, and R. L. Harlow, *Materials Research Bulletin* **29** (1994), 10.1016/0025-5408(94)90120-1.
- <sup>37</sup> D. J. Groenendijk, N. Manca, G. Mattoni, L. Kootstra, S. Gariglio, Y. Huang, E. van Heumen, and A. D. Caviglia, *Applied Physics Letters* **109** (2016), 10.1063/1.4960101.
- <sup>38</sup> Y. F. Nie, P. D. C. King, C. H. Kim, M. Uchida, H. I. Wei, B. D. Faeth, J. P. Ruff, L. Xie, X. Pan, C. Fennie, D. G. Schlom, and K. M. Shen, *Physical Review Letters* **114** (2015), 10.1103/PhysRevLett.114.016401.
- <sup>39</sup> S. Greaves, A. L. Greer, R. S. Lakes, and T. Rouxel, *Nature Materials* **10** (2011), 10.1038/NMAT3134.
- <sup>40</sup> C. Huang and L. Chen, *Advanced Materials* **28** (2016), 10.1002/adma.201601363.
- <sup>41</sup> L. Iglesias, A. Sarantopoulos, C. Magen, and F. Rivadulla, *Physical Review B* **95** (2017), 10.1103/PhysRevB.95.165138.
- <sup>42</sup> U. Aschauer, R. Pfenninger, S. M. Selbach, T. Grande, and N. A. Spaldin, *Physical Review B* **88** (2013), 10.1103/PhysRevB.88.054111.
- <sup>43</sup> S. Chikara, O. Korneta, W. P. Crummett, L. E. DeLong, P. Schlottmann, and G. Cao, *Journal of Applied Physics* **107** (2010), 10.1063/1.3362912.
- <sup>44</sup> T. Shimura, Y. Inaguma, T. Nakamura, M. Itoh, and Y. Morii, *Physical Review B* **52** (1995), 10.1103/PhysRevB.52.9143.
- <sup>45</sup> S. Boseggia, H. C. Walker, J. Vale, R. Springell, Z. Feng, R. S. Perry, M. M. Sala, S. P. C. H. M. Ronnow, and D. F. McMorrow, *Journal of Physics: Condensed Matter* **25** (2013), 10.1088/0953-8984/25/36/365101.
- <sup>46</sup> T. F. Qi, O. B. Korneta, D. E. D. Long, P. Schlottmann, W. P. Crummett, and G. Cao, *Physical Review B* **84** (2011), 10.1103/PhysRevB.84.100402.
- <sup>47</sup> F. Ye, S. Chi, B. C. Chakoumakos, J. A. Fernandez-Baca, T. Qi, and G. Cao, *Physical Review B* **87** (2013), 10.1103/PhysRevB.87.140406.
- <sup>48</sup> L. Miao, H. Xu, and Z. Q. Mao, *Physical Review B* **89** (2014), 10.1103/PhysRevB.89.035109.
- <sup>49</sup> G. Cao, Y. Xin, C. S. Alexander, J. E. Crow, P. Schlottmann, M. K. Crawford, R. Harlow, and W. Marshall, *Physical Review B* **66** (2002), 10.1103/PhysRevB.66.214412.
- <sup>50</sup> N. S. Kini, A. M. Strydom, H. S. Jeevan, C. Geibel, and S. Ramakrishnan, *Journal of Physics: Condensed Matter* **18**, 8205 (2006).
- <sup>51</sup> A. Biswas, K. S. Kim, and Y. H. Jeong, *Journal of Applied Physics* **116** (2014), 10.1063/1.4903314.
- <sup>52</sup> J. Matsuno, K. Ihara, S. Yamamura, H. Wadati, Y. Ishii, V. V. Shankar, H. Y. Kee, and H. Takagi, *Physical Review Letters* **114** (2015), 10.1103/PhysRevLett.114.247209.
- <sup>53</sup> Y. Ohuchi, J. Matsuno, N. Ogawa, Y. Kozuka, M. Uchida, Y. Tokura, and M. Kawasaki, *Nature Communications* **9** (2018), 10.1038/s41467-017-02629-3.
- <sup>54</sup> A. Tselev, R. K. Vasudevan, A. G. Gianfrancesco, L. Qiao, P. Ganesh, T. L. Meyer, H. N. Lee, M. D. Biegalski, A. P. Baddorf, and S. V. Kalinin, *ACS Nano* **9** (2015), 10.1021/acs.nano.5b00743.